

# All-Sky Dynamical Response of the Galactic Halo to the Large Magellanic Cloud

Charlie Conroy<sup>1</sup>, Rohan P. Naidu<sup>1</sup>, Nicolás Garavito-Camargo<sup>2</sup>, Gurtina Besla<sup>2</sup>, Dennis Zaritsky<sup>2</sup>, Ana Bonaca<sup>1</sup>, Benjamin D. Johnson<sup>1</sup>

**Gravitational interactions between the Large Magellanic Cloud (LMC) and the stellar and dark matter halo of the Milky Way are expected to give rise to disequilibrium phenomena in the outer Milky Way<sup>1-7</sup>. A local wake is predicted to trail the orbit of the LMC, while a large-scale over-density is predicted to exist across a large area of the northern Galactic hemisphere. Here we present the detection of both the local wake and Northern over-density (hereafter the “collective response”) in an all-sky star map of the Galaxy based on 1301 stars at  $60 < R_{\text{gal}} < 100$  kpc. The location of the wake is in good agreement with an N-body simulation that includes the dynamical effect of the LMC on the Milky Way halo. The density contrast of the wake and collective response are both stronger in the data than in the simulation. The detection of a strong local wake is independent evidence that the Magellanic Clouds are on their first orbit around the Milky Way. The wake traces the path of the LMC, which will provide insight into the orbit of the LMC, which in turn is a sensitive probe of the mass of the LMC and the Milky Way. These data demonstrate that the outer halo is not in dynamical equilibrium, as is often assumed. The morphology and strength of the wake could be used to test the nature of dark matter and gravity.**

We combined optical photometry from *Gaia* Early Data Release 3<sup>8</sup> and infrared photometry from *WISE*<sup>9</sup> to identify a pure sample of giant stars across the entire sky, excluding the Galactic plane ( $|b| < 10^\circ$ ). Photometric distances were estimated with a 10 Gyr  $[\text{Fe}/\text{H}] = -1.5$  isochrone<sup>10</sup>. Distances were converted to Galactic physical coordinates, and the final sample was selected to lie at Galactocentric distances of  $60 < R_{\text{gal}} < 100$  kpc, where simulations predict a strong signal due to the dynamical response of the LMC and where contamination from previously known structures is minimized. Selections in sky coordinates and *Gaia* proper motions were used to remove stars associated with known objects including the LMC and SMC, Milky Way disk stars, and the Sagittarius stream (see Methods

for details).

In Fig. 1a we show an equal-area Mollweide projection map of the resulting sample of 1301 stars in Galactic coordinates. The map has been smoothed by a Gaussian beam with  $\text{FWHM} = 30^\circ$  and colored by the density contrast. Grey regions indicate portions of the sky that have been masked. There are two significant overdensities spanning thousands of square degrees. The southern feature is strongest at  $l > 0^\circ$  but appears to connect directly to the LMC and SMC (as can be seen more clearly in Extended Data Fig. 3). The overdensity in the north spans nearly one quarter of the entire sky. A portion of the southern feature was previously identified as the Pisces Plume<sup>12</sup>, but the map here uncovers its full extent on the sky.

In Fig. 1b we show predictions from an N-body simulation that includes the dynamical response of the Galactic halo to the LMC<sup>2</sup>. The LMC orbit in this model matches existing constraints on the present-day position and motion of the LMC<sup>13</sup>, and has the LMC on its first passage around the Galaxy. The model shown here assumed a total Milky Way mass of  $M_{\text{halo}} = 1.2 \times 10^{12} M_\odot$  and an initial LMC mass of  $M_{\text{halo}} = 1.8 \times 10^{11} M_\odot$ . The simulated halo has been processed to match the selections applied to the data, enabling a direct comparison between the two maps. The dynamical response of the Galactic halo to the LMC has two primary components: 1) in the south, a local wake is excited behind the orbit of the LMC. This is the classic Chandrasekhar dynamical friction wake<sup>14</sup>. 2) A global, collective response is also created, and is mostly the result of the movement of the barycenter of the Galaxy in the presence of the LMC<sup>2,3,15</sup>. This collective response manifests as a large-scale overdensity in the northern sky. An important consequence of the simulation is that the dynamical response should be manifest in *both* the stars and the dark matter, and so a detection of structure in the former suggests a similar level of structure in the latter.

There are several immediate implications of Fig 1. First, the outer halo of our Galaxy is in a state of significant disequilibrium, with order unity variations in the density spanning thousands of square degrees. Most previous work attempting to constrain the outer mass distribution in the Galaxy has by necessity assumed simple equilibrium models<sup>16,17</sup>. Future studies must account for the disequilibrium now measured in the Galactic halo. Second, the very strong observed local wake is independent evidence that the Magellanic Clouds are on their

<sup>1</sup>Center for Astrophysics | Harvard & Smithsonian, Cambridge, MA, USA

<sup>2</sup>Steward Observatory, University of Arizona, 933 North Cherry Avenue, Tucson, AZ 85721, USA

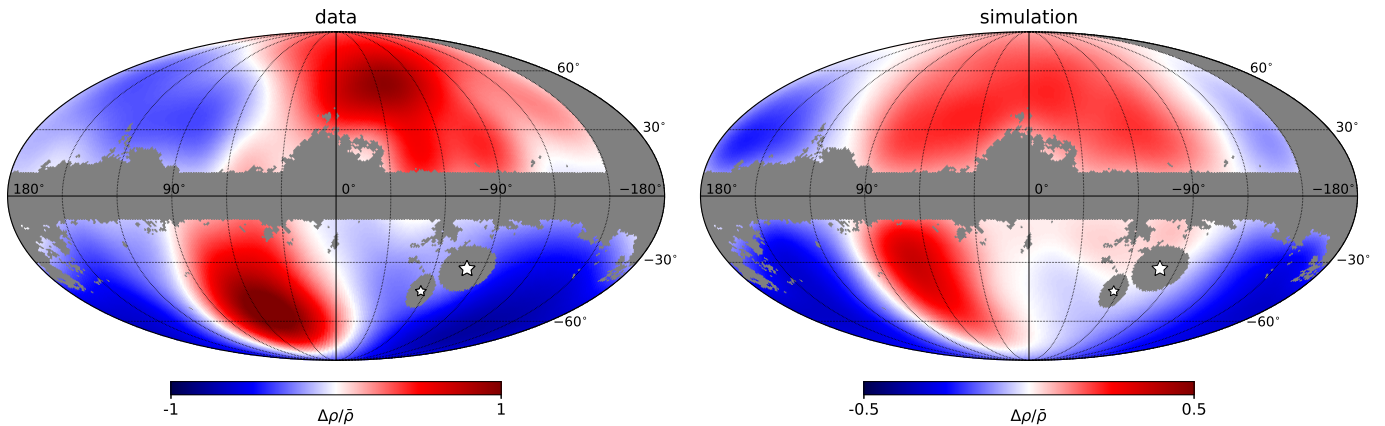


Figure 1: **Distribution of stars in the Galactic halo.** All-sky Mollweide projection maps of the density of stars at  $60 \text{ kpc} < R_{\text{gal}} < 100 \text{ kpc}$ , smoothed by a Gaussian kernel with  $\text{FWHM} = 30^\circ$ . **Left panel:** data based on K giant stars. **Right panel:** simulation that includes the dynamical response of the halo to the orbit of the LMC. Regions near the Galactic mid-plane ( $|b| < 10^\circ$ ) and the LMC and SMC, as well as regions of high extinction are masked in grey, while the positions of the LMC and SMC are marked as white stars. One arm of the Sagittarius stream has been masked in sky coordinates, as indicated by the grey region at  $b > 0^\circ$  and  $-180^\circ < l < -150^\circ$ . The overdensity in the south-west is the local wake caused by the passage of the LMC. The overdensity in the North is the collective response of the Galaxy due to the arrival of the LMC. Notice that the dynamic range of the density contrast for the simulated map is smaller than the observed map.

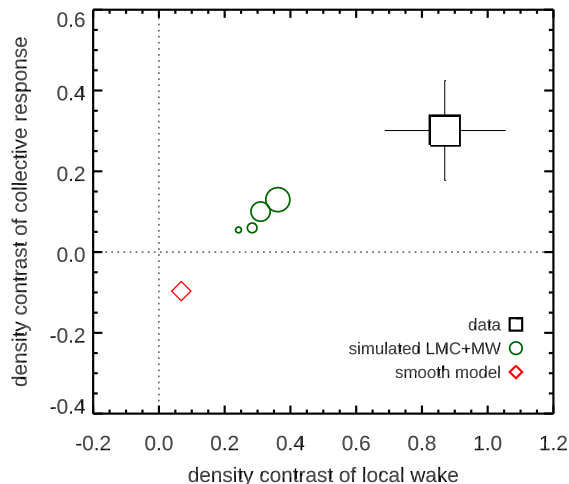


Figure 2: **Quantitative comparison between data and models.** Mean density contrasts in regions encompassing the local wake ( $-60^\circ < b < -20^\circ$ ,  $45^\circ < l < 90^\circ$ ) and the collective response ( $30^\circ < b < 60^\circ$ ,  $240^\circ < l < 300^\circ$ ) are shown along the  $x$  and  $y$  axes. There are four simulations spanning a range in LMC masses from  $0.8 - 2.5 \times 10^{11} M_\odot$  (small-to-large green circles). The smooth model<sup>11</sup> is close to zero along both axes as expected. The dotted lines indicate uniform distributions (no density contrast) on the  $x$  and  $y$  axes. The density enhancement of the local wake is measured at a significance of  $5\sigma$  (error bars on the data represent  $1\sigma$  Poisson uncertainties) and the mean density is  $1.4 \pm 0.2$  times larger in the data than in the fiducial simulation.

positions and velocities of the Clouds had also inferred a first-passage scenario for the orbits of the Clouds<sup>18</sup>, although those results are sensitive to the uncertain mass of the Galaxy. If the Clouds had undergone more than one complete orbit, the local wake would be much weaker, and perhaps not even detectable, due to destructive interference after repeated orbits, as in the case of the Sagittarius dwarf galaxy<sup>2</sup>. Third, the local wake is predicted to accurately trace the orbital path of the LMC<sup>2</sup>, and so its observed location will provide stringent new constraints on the orbit of the LMC.

In Fig. 2 we provide a quantitative comparison between observations and simulations of the strength of the local wake and collective response. Regions encompassing the local wake ( $-60^\circ < b < -20^\circ$ ,  $45^\circ < l < 90^\circ$ ) and the collective response ( $30^\circ < b < 60^\circ$ ,  $240^\circ < l < 300^\circ$ ) are defined and the mean density contrast is measured within them (using unsmoothed versions of the maps in Fig. 1). Poisson statistics are used to estimate  $1\sigma$  uncertainties. In this figure we show results for four simulations with a range of LMC masses at infall:  $(0.8, 1.0, 1.8, 2.5) \times 10^{11} M_\odot$ . The density contrast in the local wake increases with increasing LMC mass, but overall the simulations predict a density contrast lower than observed. In the data, the collective response is largely confined to  $-180^\circ < l < 0^\circ$ . Although the collective response is expected to be broadly asymmetric<sup>2</sup>, in the observed footprint the simulated collective response is approximately symmetric about  $l = 0^\circ$  (see Methods for further discussion). We also show results for a smooth stellar halo<sup>11</sup> - as expected this model shows no significant excess or deficit of stars in the wake or collective response regions.

The simulation is a genuine prediction and was not calibrated in any way to reproduce the observed features. The overall agreement between the simulation and observations, especially in the Southern hemisphere, is therefore quite striking.

first passage around the Galaxy. Previous work analyzing the

Unsurprisingly, given the large available parameter space, the agreement is not perfect. For example, the density of the local wake in the fiducial simulation is lower by a factor of  $1.4 \pm 0.2$  and the location of the peak density occurs further away from the LMC compared to the observations. In addition, the collective response in the northern hemisphere is not as asymmetric (west vs. east) in the simulation as in the data. The precise location and density of the local wake is sensitive not only to the mass of the LMC, but, because the formation of the wake is a resonant process<sup>19</sup>, is also sensitive to the orbit of the LMC and the distribution of orbits within and shape of the Milky Way halo. Furthermore, the impact of the SMC on these predictions has not yet been studied. The initial simulated stellar halo was smooth; the amplitude of the wake in a realistic halo built from mergers might be different. Exploration of this parameter space will be necessary to determine if such a large observed wake signal can be accommodated within conventional models for the Milky Way and LMC. Because the wake is sculpted by the total gravitational mass and not just the stars, its existence and detailed morphology may also provide stringent tests of non-standard dark matter (e.g., fuzzy dark matter, self-interacting dark matter)<sup>20–22</sup> and alternative gravity models<sup>23,24</sup>.

The exact location of the collective response on the sky is also sensitive to the orbit of the LMC, which is in turn sensitive to the mass of the Milky Way. As with the local wake, the collective response is sensitive to the distribution of orbits within the Galactic halo. Simulations that explore these variables will be necessary to see if the observed location of the collective response can be reproduced.

The Magellanic stream is a vast structure of cold gas trailing and originating from the LMC and SMC<sup>25,26</sup>. Simulations predict a corresponding stellar stream in the vicinity of the gaseous stream<sup>27,28</sup>, although its location and mass content is uncertain. The stellar stream is predicted to be narrower on the sky than the local wake<sup>2</sup> and to reside at  $R_{\text{gal}} > 100$  kpc at the location of the local wake<sup>29</sup>. There have recently been detections of cold stellar structure in this region of the sky, perhaps associated with the Magellanic system in some way<sup>30,31</sup>. In the Methods we provide an un-smoothed version of Fig. 1a which does not reveal a colder feature that could be associated with a stream. Kinematic information should be definitive – a stellar stream, if one exists, should have distinct kinematic behavior compared to the local wake.

Simulations that include the effect of the LMC on the Galactic halo<sup>2,3,5</sup> predict large radial and tangential velocity differences across the sky due to the dynamical response of the halo to the LMC, with amplitudes exceeding  $45 \text{ km s}^{-1}$ . The sample presented here will be ideal for measuring the velocity signal from spectroscopy and proper motions, as nearly all stars are brighter than  $G = 17.5$ . Independent work has recently detected the predicted velocity signatures<sup>32,33</sup>. These detections provide strong corroboration that the density variations reported here are due to the dynamical response of the Galaxy to the presence of the Magellanic Clouds. The joint mapping and modeling of the density and kinematic signatures is the next step in uncovering the complex phase space structure imprinted by the Magellanic Clouds in the outer Galaxy.

1. Laporte, C. F. P., Gómez, F. A., Besla, G., Johnston, K. V., & Garavito-Camargo, N. Response of the Milky Way's disc to the Large Magellanic Cloud in a first infall scenario *Mon. Not. R. Astron. Soc.* **473**, 1218–1230 (2018).
2. Garavito-Camargo, N. *et al.* Hunting for the Dark Matter Wake Induced by the Large Magellanic Cloud *Astrophys. J.* **884**, 51 (2019).
3. Petersen, M. S. & Peñarrubia, J. Reflex motion in the Milky Way stellar halo resulting from the Large Magellanic Cloud infall *Mon. Not. R. Astron. Soc.* **494** L11–L16 (2020).
4. Erkal, D., Belokurov, V. & Parkin, D. L. Equilibrium models of the Milky Way mass are biased high by the LMC *Mon. Not. R. Astron. Soc.* **498** 5574–5580 (2020).
5. Cunningham, E. C. *et al.* Quantifying the Stellar Halo's Response to the LMC's Infall with Spherical Harmonics. *Astrophys. J.* **898**, 4 (2020).
6. Tamfal, T. *et al.* Revisiting dynamical friction: the role of global modes and local wakes arXiv:2007.13763 (2020).
7. Garavito-Camargo, N. *et al.* Quantifying the impact of the Large Magellanic Cloud on the structure of the Milky Way's dark matter halo using Basis Function Expansions arXiv:2010.00816 (2020).
8. Lindegren, L. *et al.* Gaia Early Data Release 3: The astrometric solution arXiv:2012.03380 (2020).
9. Schlafly, E. F., Meisner, A. M. & Green, G. M. The unWISE Catalog: Two Billion Infrared Sources from Five Years of WISE Imaging *Astrophys. J. Supp.* **240**, 30 (2019).
10. Choi, J. *et al.* Mesa Isochrones and Stellar Tracks (MIST). I. Solar-scaled Models *Astrophys. J.* **823**, 102 (2016).
11. Rybizki, J. *et al.* A Gaia DR2 Mock Stellar Catalog *Publ. Astron. Soc. Pac.* **130**, 074101 (2018).
12. Belokurov, V. *et al.* The Pisces Plume and the Magellanic wake *Mon. Not. R. Astron. Soc.* **488**, L47–L52 (2019).
13. Kallivayalil, N., van der Marel, R. P., Besla, G., Anderson, J. & Alcock, C. Third-epoch Magellanic Cloud Proper Motions. I. Hubble Space Telescope/WFC3 Data and Orbit Implications *Astrophys. J.* **764**, 161 (2013).
14. Chandrasekhar, S. Dynamical Friction. I. General Considerations: the Coefficient of Dynamical Friction. *Astrophys. J.* **97**, 255 (1943).
15. Gómez, F. A. *et al.* And Yet it Moves: The Dangers of Artificially Fixing the Milky Way Center of Mass in the Presence of a Massive Large Magellanic Cloud *Astrophys. J.* **802**, 128 (2015).
16. Williams, A. A., Belokurov, V., Casey, A. R. & Evans, N. W. On the run: mapping the escape speed across the Galaxy with SDSS *Mon. Not. R. Astron. Soc.* **468**, 2359–2371 (2017).
17. Deason, A. J. *et al.* The local high-velocity tail and the Galactic escape speed *Mon. Not. R. Astron. Soc.* **485**, 3514–3526 (2019).
18. Besla, G. *et al.* Are the Magellanic Clouds on Their First Passage about the Milky Way? *Astrophys. J.* **668**, 949–967 (2007).
19. Weinberg, M. D. Dynamics of an interacting luminous disc, dark halo and satellite companion *Mon. Not. R. Astron. Soc.* **299**, 499–514 (1998).
20. Furlanetto, S. R. & Loeb, A. Constraining the Collisional Nature of the Dark Matter through Observations of Gravitational Wakes *Astrophys. J.* **565**, 854–866 (2002).
21. Hui, L., Ostriker, J. P., Tremaine, S. & Witten, E. Ultralight scalars as cosmological dark matter *Phys. Rev. D* **95**, 043541 (2017).
22. Lancaster, L. *et al.* Dynamical friction in a Fuzzy Dark Matter universe *J. Cosmo. Astropart. Phys.* **2020**, 001 (2020).
23. Ciotti, L. & Binney, J. Two-body relaxation in modified Newtonian dynamics *Mon. Not. R. Astron. Soc.* **351**, 285–291 (2004).
24. Nipoti, C., Ciotti, L., Binney, J. & Londrillo, P. Dynamical friction in modified Newtonian dynamics *Mon. Not. R. Astron. Soc.* **386** 2194–2198 (2008).
25. D'Onghia, E. & Fox, A. J. The Magellanic Stream: Circumnavigating the Galaxy *Annu. Rev. Astron. Astrophys.* **54**, 363–400 (2016).
26. Lucchini, S. *et al.* The Magellanic Corona and the formation of the Magellanic Stream *Nature* **585**, 203–206 (2020).
27. Gardiner, L. T. & Noguchi, M. N-body simulations of the Small Magellanic Cloud and the Magellanic Stream *Mon. Not. R. Astron. Soc.* **278**, 191–208 (1996).

# METHODS

28. Diaz, J. D. & Bekki, K. The Tidal Origin of the Magellanic Stream and the Possibility of a Stellar Counterpart *Astrophys. J.* **750**, 36 (2012).
29. Besla, G., Hernquist, L. & Loeb, A. The origin of the microlensing events observed towards the LMC and the stellar counterpart of the Magellanic stream *Mon. Not. R. Astron. Soc.* **428**, 2342–2365 (2013).
30. Deason, A. J., Belokurov, V. & Koposov, S. E. To the Galactic Virial Radius with Hyper Suprime-Cam *Astrophys. J.* **852**, 118 (2018).
31. Zaritsky, D. *et al.* Discovery of Magellanic Stellar Debris in the H3 Survey *Astrophys. J.* **905**, L3 (2020).
32. Petersen, M. S. & Peñarrubia, J. Detection of the Milky Way reflex motion due to the Large Magellanic Cloud infall *Nature Astronomy* (2020).
33. Erkal, D. *et al.* Detection of the LMC-induced sloshing of the Galactic halo arXiv:2010.13789 (2020).

**Acknowledgements** We thank both referees for their constructive feedback. C.C. is partially supported by the Packard Foundation. R.P.N. gratefully acknowledges an Ashford Fellowship and Peirce Fellowship granted by Harvard University. G.B. and N.G.-C. are supported by HST grant AR 15004, NASA ATP grant 17-ATP17-0006, NSF CAREER AST-1941096. A.B. acknowledges support from NASA through HST grant HST-GO-15930. All the simulations were run on El-Gato super computer which was supported by the National Science Foundation under Grant No. 1228509. We have made use of data from the European Space Agency mission Gaia (<http://www.cosmos.esa.int/gaia>), processed by the Gaia Data Processing and Analysis Consortium (DPAC; see <http://www.cosmos.esa.int/web/gaia/dpac/consortium>). Funding for DPAC has been provided by national institutions, in particular the institutions participating in the Gaia Multilateral Agreement. This publication makes use of data products from the *Wide-field Infrared Survey Explorer*, which is a joint project of the University of California, Los Angeles, and the Jet Propulsion Laboratory/California Institute of Technology, and NEOWISE, which is a project of the Jet Propulsion Laboratory/ California Institute of Technology. *WISE* and NEOWISE are funded by the National Aeronautics and Space Administration.

**Author Contributions** C.C. and R.P.N. jointly conceived of the project. C.C. led the analysis of the data. N.G.-C. and G.B. provided the simulation data and aided in its interpretation. All authors contributed to aspects of the analysis and to the writing of the manuscript.

**Author Information** Reprints and permissions information is available at [npg.nature.com/reprintsandpermissions](http://npg.nature.com/reprintsandpermissions). Correspondence and requests for materials should be addressed to C.C. ([cconroy@cfa.harvard.edu](mailto:cconroy@cfa.harvard.edu)).

**Data Availability** The K giant catalog used in this paper is available at <https://doi.org/10.7910/DVN/2D1H8J>.

**Code Availability** We have opted not to make the code used in this manuscript available because the data reduction and analysis is straightforward and can be easily reproduced following the methods described herein.

## Identification of giants

In order to study the outer stellar halo across the entire sky we need a means of identifying, with high purity, a sample of giant stars based solely on all-sky photometry. Previous work<sup>34,35</sup> employed 2MASS  $JHK_s$  photometry to identify M giant stars by relying on the pressure-sensitivity of continuous opacity sources (mostly  $H^-$ ). However, the relatively shallow depth of 2MASS precluded a detailed view of the outer halo (our sample of stars is largely confined to  $K_s > 13$  while previous work was limited to  $K_s < 13$ ). We recently presented a photometric selection technique<sup>36</sup> based on Pan-STARRS and *WISE* colors that efficiently identified K giants to  $W1 = 15$ . The downside to this approach is that Pan-STARRS is not an all-sky survey. We therefore decided to explore the possibility of using *Gaia* and *WISE* photometry in order to select giants across the entire sky. In order to correct for dust extinction we adopt the following reddening coefficients:  $A_{BP}/E(B - V) = 3.0$ ,  $A_{RP}/E(B - V) = 1.92$ , and  $A_{W1}/E(B - V) = 0.18$ . The normalization of the standard  $E(B - V)$  dust map<sup>37</sup> is reduced by 14% following more recent work<sup>38</sup>. We also make two selections on *Gaia* quality flags:  $ruwe < 1.4$  and  $3\sigma$  clipping of the corrected BP and RP flux excess factor  $C^*$ <sup>39</sup>. We also apply a parallax selection of  $\pi < 0.2$  mas to remove obvious foreground stars, using the corrected parallaxes from *Gaia*<sup>40</sup>. For the *WISE* data, we restrict to  $12 < W1 < 15$ , a magnitude range that is nearly 100% complete<sup>9</sup> and has formal uncertainties of 0.01 mag at the faint end of this range.

Extended Data Fig. 1 shows the distribution in  $BP - RP$  and  $RP - W1$  colors for stars with  $12 < W1 < 15$  at high Galactic latitudes. This specific subsample was chosen to minimize Galactic reddening. Two sequences are clearly visible, with the upper and lower branches containing giants and dwarfs, respectively. We fit a polynomial to the giant sequence:

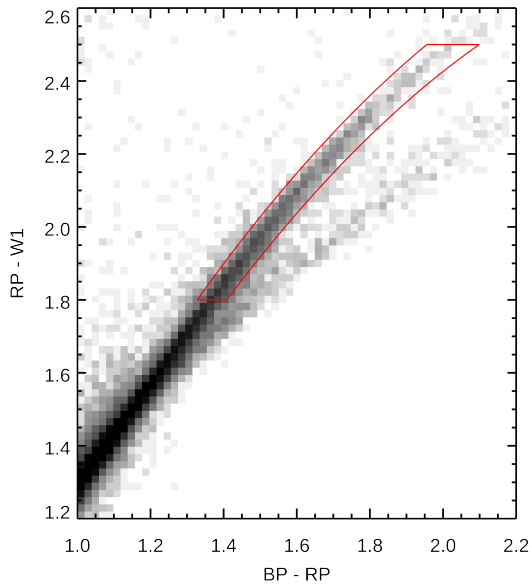
$$(RP - W1)_{\text{fid}} = -0.9134 + 2.5985 (BP - RP) - 0.4518 (BP - RP)^2 \quad (1)$$

and the red lines are defined by  $(RP - W1)_{\text{fid}} + 0.06$  and  $(RP - W1)_{\text{fid}} - 0.05$ . We also impose a limit of  $1.8 < (RP - W1) < 2.5$ . This selection is applied to an all-sky catalog of *Gaia* and *WISE* cross-matched sources. For a metallicity of  $[Fe/H] = -1.5$ , this color range corresponds to red giants with  $3800 < T_{\text{eff}} < 4400$  K, i.e., K giant stars.

Distances are estimated for these giants by using MIST stellar isochrones<sup>10</sup>. Specifically, we select red giant branch stars from a 10 Gyr,  $[Fe/H] = -1.5$  model and fit a quadratic function between the  $BP - RP$  color and the  $W1$  absolute magnitude:

$$M_{W1} = 11.547 - 17.117 (BP - RP) + 3.9329 (BP - RP)^2 \quad (2)$$

This equation is used to estimate distances for all stars in the catalog. Distances based on a single color will not be very accurate as good photometric distances require some knowledge of the age and metallicity, both of which we have fixed here. The stellar halo is widely believed to be old, and even factors of two change in the adopted age changes the inferred distance by only  $\approx 7\%$ . The metallicity has a larger impact on the inferred distances. For example, assuming a fixed color of  $BP - RP = 1.4$ ,



### Extended Data Figure 1 | Photometric selection of giants.

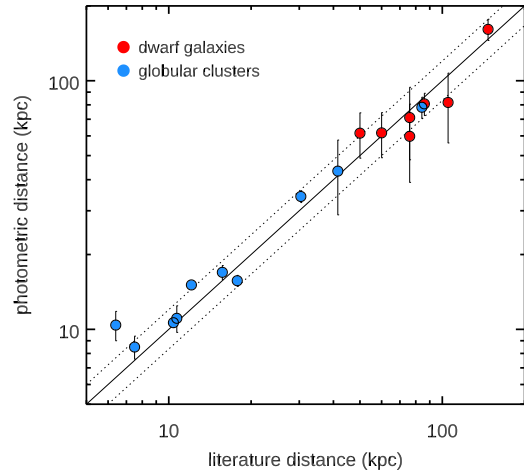
Color-color diagram for stars at high Galactic latitude ( $b > 45^\circ$ ) with *Gaia* parallax  $\pi < 0.1$  mas. Two sequences are clearly visible, with the upper branch being associated with giant stars, and the lower with dwarf stars. The red lines mark the selection boundary used in this work.

increasing the metallicity to  $[\text{Fe}/\text{H}] = -1.0$  would result in 25% closer distances, while assuming  $[\text{Fe}/\text{H}] = -2.0$  would place the distances 14% further away compared to our fiducial isochrone. We have adopted  $[\text{Fe}/\text{H}] = -1.5$  based on the fact that the mean metallicity of the halo is  $\langle [\text{Fe}/\text{H}] \rangle = -1.2$  with some evidence for a slightly more metal-poor halo at  $R_{\text{gal}} > 50$  kpc<sup>42</sup>. We emphasize that precise distances are not required in this work – they are simply used to place stars in broad radial bins.

The strongest test of these photometric distances comes from direct comparison to literature distances. This test is provided in Extended Data Fig. 2. We identified stars in our giant catalog that are spatially associated with dwarf satellite galaxies and globular clusters (GCs). In the former category, we found significant numbers of stars associated with Fornax, Draco, Sculptor, Carina, Ursa Minor, the LMC and SMC. For the GCs, we found nine objects with 10 or more stars in our catalog with  $12 < W1 < 14$ . The figure compares the median photometric distance for each source to known literature values<sup>41,43</sup>. The agreement is good at the  $\pm 20\%$  level, which gives confidence that the photometric distances are both accurate and reasonably precise.

### Removal of structure and map-making

Starting with the catalog of giants, we identify the parent sample as stars that satisfy a magnitude selection of  $12 < W1 < 15$  and a *Gaia* parallax selection of  $\pi < 0.2$  mas (we use the corrected parallaxes available in *Gaia* EDR3<sup>40</sup>). We also remove



### Extended Data Figure 2 | Test of Photometric Distances.

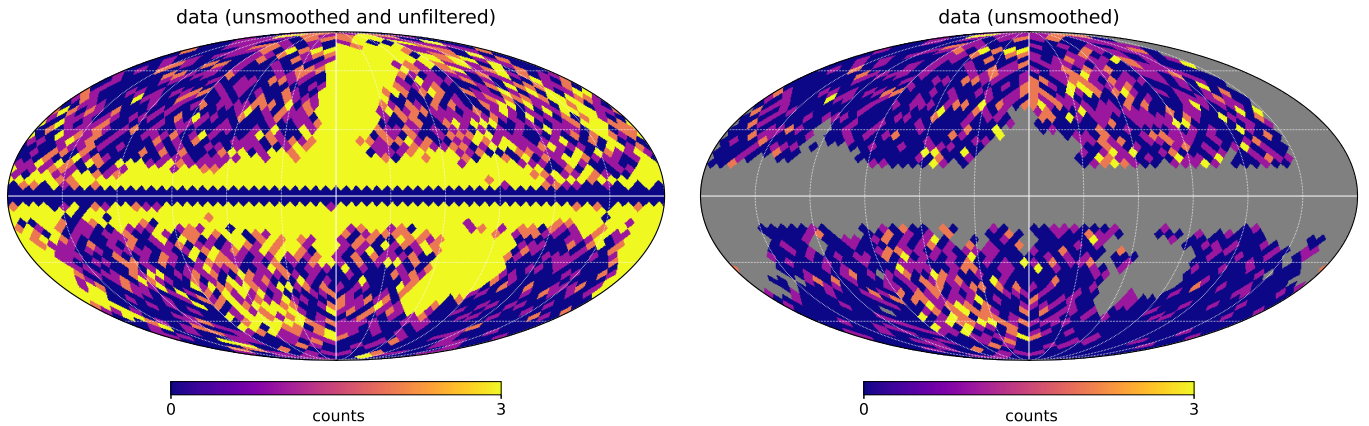
Comparison of our photometric distances against literature values for satellite galaxies around the Milky Way (red) and globular clusters (blue). Error bars represent the  $1\sigma$  scatter in the photometric distances and dotted lines mark  $\pm 20\%$  about the one-to-one line. The dwarf galaxies include Fornax, Draco, Sculptor, Carina, Ursa Minor, and the LMC and SMC, and span average metallicities from  $[\text{Fe}/\text{H}] \approx -0.5$  (LMC) to  $-2.2$  (Ursa Minor)<sup>41</sup>.

stars with  $E(B - V) > 0.3$  (regions with such large reddening are masked in the all sky maps). We then select stars with Galactocentric distances of  $60 < R_{\text{gal}} < 100$  kpc, and further require stars to lie off the Galactic plane ( $|b| > 10^\circ$ ). We also remove stars clearly associated with the dwarf galaxies and GCs mentioned above. This sample comprises 146,926 stars (the vast majority of which are associated with the LMC and SMC). Extended Data Fig. 3a shows the density distribution in Galactic coordinates of this sample in a Mollweide projection. Each pixel has an area of 13.4 sq. deg and the color is proportional to the number of stars in each pixel.

There is significant structure throughout the sky. The brightest features in this map are associated with the LMC and SMC (lower right), the Galactic disk and bulge (center) and the Sagittarius stream (center-north, and at the edges of the map in the South). The overdensities associated with the local wake and collective response are clearly visible in this raw map. However, in an attempt to isolate the features of interest we have selected various populations for removal on the basis of sky coordinates and proper motions.

The LMC and SMC are removed via selections in Galactic ( $l, b$ ) space. In the case of the LMC, a circular region with radius of  $8^\circ$  centered on the LMC was excised from the catalog. For the SMC, an ellipse with semi-major and minor axes of  $3.2^\circ$  and  $2.5^\circ$  centered on the SMC was used to remove stars (additional LMC and SMC stars beyond the Galactic coordinate cut are removed via the proper motion selection below). These selections reduce the catalog to 5,007 stars.

Proper motions offer an efficient means by which we can



**Extended Data Figure 3 | Maps of un-smoothed star counts.** Mollweide projection maps of the observed sample of giants with pixels of size 13.4 sq. deg. **Left panel:** map with no masking of known structure, either in sky coordinates or proper motions. The two main features identified here, the transient wake and the collective response, are still clearly visible even in this unfiltered map. The LMC and SMC appear in the lower right as a merged region of high density. Other features include the stellar disk+bulge in the center, and the Sagittarius stream both in the north-center and lower left and right. **Right panel:** map showing the filtered catalog used in Fig 1a.

remove structure unassociated with the diffuse halo. We work with solar reflex motion-corrected proper motions. The effect of the reflex motion correction is shown in Extended Data Fig. 4. The upper left panel shows the raw proper motions while the upper right shows the reflex-corrected proper motions. The lower left panel shows the sample at  $b > 0^\circ$  and  $|b_{\text{Sgr}}| < 15^\circ$  where  $b_{\text{Sgr}}$  is the latitude in the frame of the Sagittarius orbital plane<sup>49</sup>. The dense clump contains the Sagittarius stream in the North at  $l \sim 0^\circ$ . The red box is used to remove these stars and is defined by  $\mu_\alpha > -1.3 \text{ mas yr}^{-1}$ ,  $-0.4 < \mu_\delta < 0.3 \text{ mas yr}^{-1}$ , and  $\mu_\delta > 1.7\mu_\alpha + 0.4 \text{ mas yr}^{-1}$  for  $b > 0^\circ$  and  $|b_{\text{Sgr}}| < 15^\circ$ . The remaining Northern arm of the Sagittarius stream is removed by simply masking the region  $b > 0^\circ$  and  $180^\circ < l < 210^\circ$  (it has low proper motion and so cannot be easily isolated from the rest of the halo via proper motion selections).

The Sagittarius selections above reduce the sample to 2,744 stars. A final selection in proper motion space is indicated by the blue circles in the bottom panels of Extended Data Fig. 4:  $\mu_\alpha^2 + (\mu_\delta + 0.1)^2 < 0.5^2$  (in units of  $\text{mas yr}^{-1}$ ). This selection removes disk stars, LMC and SMC stars beyond the on-sky selection, the Sgr dSph, and other Sgr arms, and reduces the sample to 1301 stars. Of the stars removed with this selection, 520 are associated with the LMC and SMC and 78 with the Sgr dSph. The rest are associated with either a southern arm of Sgr or are confined to  $|b| < 20^\circ$  (these are disk stars with incorrect photometric distances, likely due to their very different metallicities). We note that the median proper motion uncertainty of the sample of 2,744 stars is 0.07 and only 110 stars have an uncertainty in either RA or DEC of  $> 0.15 \text{ mas yr}^{-1}$ .

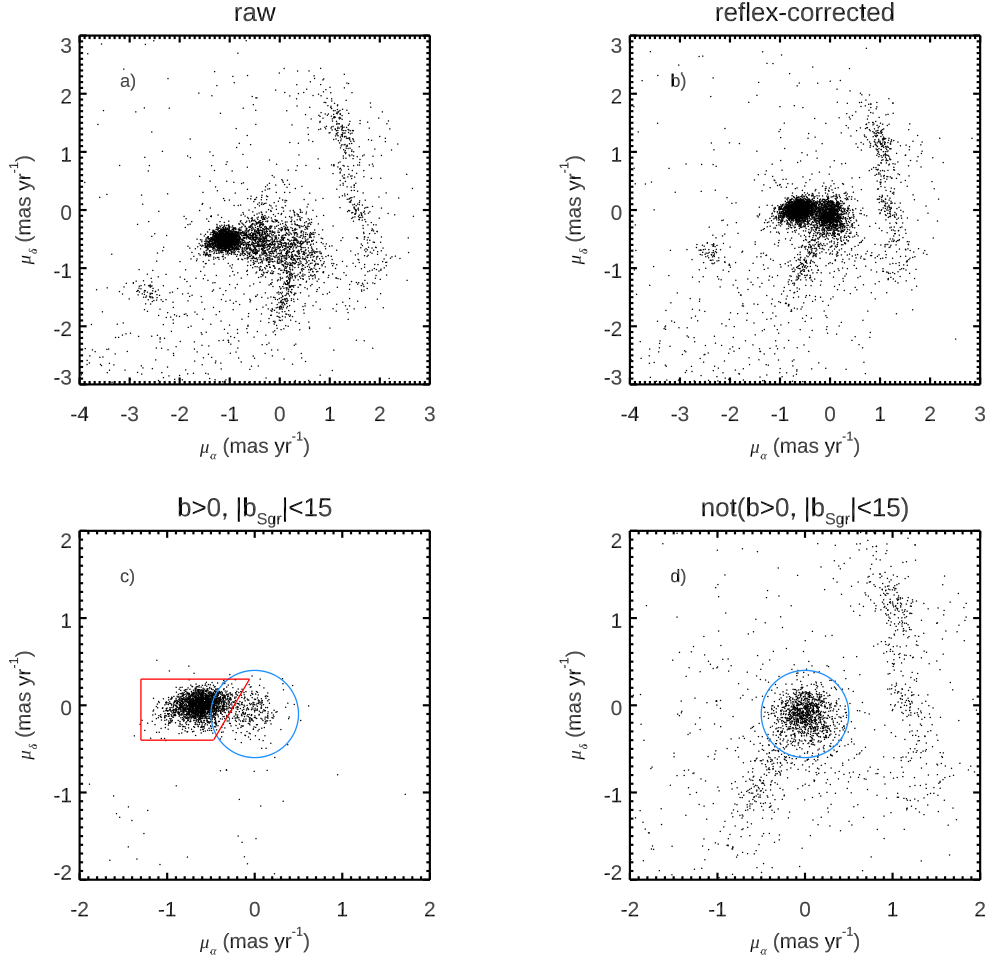
The final catalog of 1301 stars is available for download at <https://doi.org/10.7910/DVN/2D1H8J>. Ex-

<sup>44</sup> We adopt the Galactocentric frame implemented in *Astropy* v4.0 which has the following parameters:  $R_0 = 8.122 \text{ kpc}$  <sup>45</sup>,  $[V_{R,\odot}, V_{\phi,\odot}, V_{Z,\odot}] = [-12.9, 245.6, 7.78] \text{ km s}^{-1}$  <sup>46</sup>,  $Z_\odot = 20.8 \text{ pc}$  <sup>47</sup>. We use the *gala*<sup>48</sup> package *reflex.correct* by setting radial velocities to zero to account for the imprint of the solar motion on our proper motions.

tended Data Fig. 3b shows the distribution of the final clean catalog. Comparison between the two panels reveals that the various selections have a small impact on the regions of the sky containing the local wake and the collective response. Importantly, both of these features are visible in the raw, un-smoothed map. Extended Data Fig. 5 shows an annotated map of the final sample, including the orbit of the LMC (white) and the regions used to define the number counts used in Fig. 2.

In an effort to provide a direct comparison between the data and models we have applied the exact same selection criteria outlined above to the models. In particular, the sky-based selections (including the LMC, SMC, Galactic plane, and locations where  $E(B - V) > 0.3$ ) are applied as a spatial mask in the maps. Selections in (solar reflex-corrected) proper motions are applied within the catalogs. An exception to this is the selection of the Northern Sagittarius arm in proper motion space; this selection is only applied in the data. We do this because, while the selection is very clean in data space, the model halo particles are somewhat kinematically “hotter” than the data and so this selection would remove a larger number of model halo particles. We also re-sample the models to follow the same distribution in  $R_{\text{gal}}$  as the data, and have applied a 20% uncertainty to heliocentric distances to mimic our photometric distance uncertainties.

The following steps were taken to compute smoothed maps (as in e.g., Fig. 1). First, we bin the stars into pixels. Second, we apply the spatial mask. Third, for the non-masked pixels we compute the average density and divide the map by that average (and then subtract one to compute the density contrast). Fourth, we smooth the map by a Gaussian kernel. Smoothing a masked map creates challenges near the masked regions. As we are using a continuous kernel, we opted to simply set the masked regions to 0.0 for the masking procedure (which effectively means that we assume mean density for the masked regions). This is the default behavior of the *healpy*<sup>50</sup> routines used in this work.



**Extended Data Figure 4 | Proper motions of the halo sample.** **a:** proper motions of the K giants at  $60 < R_{\text{gal}} < 100$  kpc with  $12 < W1 < 15$  and the LMC and SMC removed via on-sky selection. **b:** solar reflex-corrected proper motions. Notice the much tighter distribution of stars near (0,0). In this panel the Sagittarius dSph is visible at  $(-2.5, -0.7)$ , LMC and SMC stars not removed by the on-sky selection are visible as a narrow vertical vertical strip at  $\mu_{\alpha} \gtrsim 0.5$  mas yr $^{-1}$ . The Northern Sagittarius arm is the large overdensity at  $(-0.7, 0.0)$ , and a Southern arm of Sagittarius is the diagonal cluster of points at  $\mu_{\delta} < -0.5$  mas yr $^{-1}$ . **c:** reflex-corrected proper motions focusing on the region of the sky containing the Northern Sagittarius arm at  $l \sim 0^{\circ}$ . The red box indicates our selection for removing this feature. **d:** stars not in the selection shown in panel **c**. Our selection for low proper motion stars is indicated by a blue circle in **c, d**.

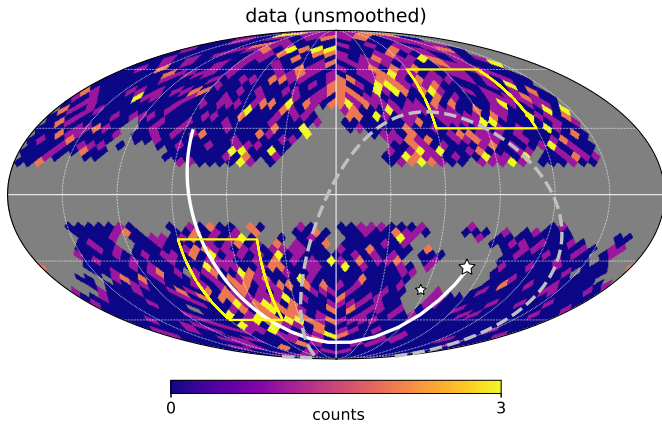
Finally, the mask is re-applied to the maps after smoothing to avoid the appearance of the data “bleeding” into the masked regions. We emphasize that the exact same procedure was applied to both the data and models, enabling a robust comparison.

Extended Data Fig. 6 shows the cumulative effect of these selections on a smooth model of the Milky Way<sup>11</sup>. This model includes an oblate power-law stellar halo with ellipticity  $\epsilon = 0.76$  that is aligned with the disk plane. The map in the left panel shows the total sample, which is uniform and symmetric about both N-S and E-W axes. The concentration of stars toward the mid-plane is a reflection of the oblate shape of the stellar halo. The map in the right panel shows the model after the selections have been applied. The proper motion selection has a minor effect on the spatial distribution of the smooth model.

### The stellar halo probed by RR Lyrae

If the observed overdensities in the Northern and Southern hemispheres are indeed due to the dynamical effect of the LMC, then a clear prediction is that the overdensities should be visible in all distant halo populations that probe the “smooth” halo (i.e., neglecting structures obviously associated with unrelaxed debris). Here we test this prediction using RR Lyrae. These stars are low metallicity variable stars whose periods can be used to infer distances to a precision of  $\approx 3\%$ <sup>51</sup>. Here we use the public RR Lyrae catalog based on Pan-STARRS data<sup>51</sup> that reach distances of  $> 100$  kpc.

We select stars with  $60 < R_{\text{gal}} < 100$  kpc, focusing on the RRAb subtype with a score of  $> 0.8$ , which have more accurate parameters. The resulting map is shown in Extended Data Fig. 7, which can be compared directly to Extended Data Fig. 3 (right panel). There are overall more RR Lyrae than K giants



**Extended Data Figure 5 | An annotated map of the outer halo.** As in Extended Data Fig. 3 (right panel), now shown with the predicted orbit of the LMC (solid white line), a line at  $\text{Dec.} = -25^\circ$  (grey dashed line, marking the approximate limit of Northern hemisphere surveys), and the locations of the two regions used to measure density ratios in Fig. 2 (solid yellow lines). The yellow region in the North measure the collective response while the yellow region in the South measures the local wake.

(as we have defined them here), so the range of the color bar is larger in the former figure. The Pan-STARRS Survey is restricted to  $\text{Dec.} > -30^\circ$ , so the map is missing data in the lower right quadrant. We have also masked  $|b| < 10^\circ$ , regions with  $E(B-V) > 0.3$ , and  $|b_{\text{Sgr}}| < 15^\circ$  (for  $b > 0^\circ$ ). This last selection was imposed because the RR Lyrae are too faint to have high quality *Gaia* proper motions ( $G \approx 20$ ), and as a consequence we could not excise the Sagittarius stream from the maps with the proper motion cuts used for the K giants. In this map one sees clearly the local wake in the Southern hemisphere (first reported as the Pisces Plume<sup>12</sup>) at a location that is in good agreement with the K giant sample. Owing to the  $\text{Dec.} = -30^\circ$  limit and the Sagittarius mask the RR Lyrae do not probe the overdensity at  $b > 0^\circ$ ,  $-180^\circ < l < 0^\circ$  as completely as in the K giant sample. Nonetheless, an overdensity is clearly visible in that region.

We provide a quantitative comparison between the RR Lyrae and K giant maps in the right panel of Extended Data Fig. 7 (cf. Fig. 2). Here we have computed the density contrast in the local wake and collective response regions, including only those pixels not masked. Because the RR Lyrae map is much less complete than the K giants, it is not possible to estimate a robust global mean density from the former. We therefore normalize the RR Lyrae map to the K giant map using a large region that is well-sampled by both maps ( $30^\circ < b < 60^\circ$ ,  $30^\circ < l < 120^\circ$ ). The density contrast of the collective response computed from the RR Lyrae is statistically indistinguishable from the measurement based on the K giant sample. However, the local wake is 50% stronger in the RR Lyrae sample. The reasons for this are unclear. The distance distribution of the RR Lyrae is weighted toward greater distances than the K giants, so the maps are not probing exactly the same radial distribution. We caution that the

densities are sensitive to our renormalization procedure.

Further progress could be made employing an all-sky map of RR Lyrae. *Gaia* Data Release 2 provided such a sample<sup>52,53</sup>. However, these maps are incomplete at the depths necessary to detect RR Lyrae at  $> 60$  kpc ( $G \approx 20$ ), driven largely by the *Gaia* scanning pattern<sup>54</sup>. For example, the local wake is not clearly visible in the *Gaia* RR Lyrae catalog despite the fact that it is so prominent in the Pan-STARRS data at  $> 60$  kpc. Future data releases from *Gaia* will hopefully reach the depths necessary to deliver complete samples of RR Lyrae in the outer halo.

### Simulation details

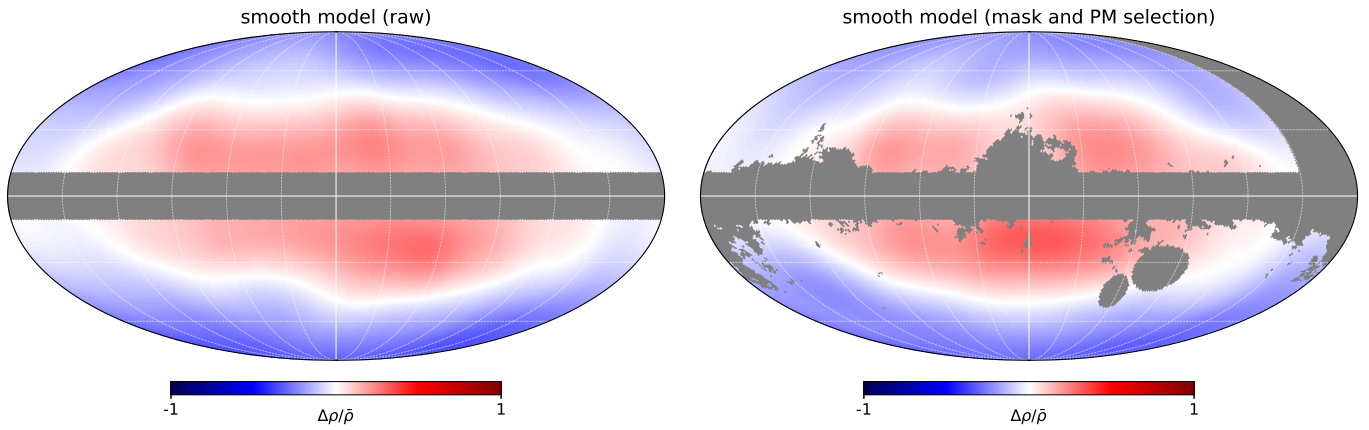
The simulations shown here were initialized with a spherical dark matter halo following a Hernquist profile<sup>55</sup>, a stellar disk, and a stellar bulge with masses of  $1.54 \times 10^{12} M_\odot$ ,  $5.78 \times 10^{10} M_\odot$ , and  $0.9 \times 10^{10} M_\odot$  respectively. Each particle has a mass of  $m_p = 1.57 \times 10^4 M_\odot$ . One model of the MW has isotropic halo kinematics while the other has a radially biased kinematic profile. The 4 LMC models were initialized with a spherical dark matter Hernquist profile with total halo masses of 0.8, 1, 1.8,  $2.5 \times 10^{11} M_\odot$ . The scale length of each of the LMC halos was chosen to match the observed rotation curve of the LMC within 9 kpc. Detailed parameters for these simulations can be found in Table 1 of the original simulation paper<sup>2</sup>. All the initial conditions for the halos were built using GAlIC<sup>56</sup>. The N-body simulations were run with P-gadget3. The initial conditions for the orbit of the LMC were found iteratively until the present-day position and velocity of the LMC was within  $2\sigma$  of the present-day observed properties of the LMC.

In this work we have utilized the raw dark matter particle data to apply a simple re-weighting scheme to match the observed density profile. The left panel of Extended Data Fig. 8 shows the  $N$ -body simulation presented in Fig. 1, now without any selections, aside from matching the density profile of the data and selecting stars with  $60 < R_{\text{gal}} < 100$  kpc. The right panel shows the same simulation now viewed from an observer placed at the Galactic center. This perspective provides a sharper distinction between the local wake and collective response<sup>2</sup>, but we opted not to make the observed maps in this way owing to the complex mapping of the Galactic reddening selection in this projection.

Another approach to constructing a mock stellar halo from these simulations is available for these simulations<sup>2</sup> and was built in equilibrium with the dark matter halo, given a specified stellar density and velocity dispersion profile using a weighing scheme designed to reproduce the observed density profile of the stellar halo. We have compared our mock stellar halo to this alternative approach and find very similar results.

The detailed structure of the halo response to the passage of the LMC has been recently quantified using Basis Function Expansions<sup>7</sup>. The halo response to the LMC has a strong amplitude in odd  $l$  modes. In contrast, triaxial, oblate and prolate halos have no odd  $l$  terms, only even terms. As such, the deformations to the MW halo caused by the LMC cannot be mimicked by a triaxial halo.





**Extended Data Figure 6 | Predicted density distribution of a smooth model.** The model<sup>11</sup> has a smooth (oblate) stellar halo. **Left panel:** the unfiltered smooth model. **Right panel** the smooth model with the same selection criteria as used in the data, including various coordinate and proper motion cuts. Both maps have been smoothed by a Gaussian with FWHM=30°. Unlike the data this map shows no obvious structure.

### A tilted halo?

The observed all-sky map of halo stars shown in Fig. 1a displays a degree of symmetry in the sense that the overdensities are confined to the south-west and north-east. We explore in this section the possibility that the observed density variation could be due to a smooth tilted stellar halo instead of our preferred interpretation of the impact of the LMC.

Extended Data Fig. 9 shows a smooth, tilted triaxial halo whose parameters were optimized (by hand) to mimic the observations in Fig. 1a. Specifically, the model has axial ratios of 0.2 (minor-to-major axes) and 0.6 (intermediate-to-major axes) and is rotated 60° anti-clockwise along the y-axis. Note that while this model reproduces some of the basic features of the data, in detail there are significant differences in both the Southern and Northern hemispheres that leads us to disfavor this interpretation of the data. Moreover, independent results based on kinematics of the stellar halo also favor the LMC dynamical response interpretation of the observed outer stellar halo<sup>32,33</sup>.

34. Majewski, S. R., Skrutskie, M. F., Weinberg, M. D. & Ostheimer, J. C. A Two Micron All Sky Survey View of the Sagittarius Dwarf Galaxy. I. Morphology of the Sagittarius Core and Tidal Arms *Astrophys. J.* **599**, 1082–1115 (2003).

35. Koposov, S. E. *et al.* Exposing Sgr tidal debris behind the Galactic disc with M giants selected in WISE $\cap$ 2MASS *Mon. Not. R. Astron. Soc.* **446**, 3110–3117 (2015).

36. Conroy, C. *et al.* They Might Be Giants: An Efficient Color-based Selection of Red Giant Stars *Astrophys. J. Let.* **861**, L16 (2018).

37. Schlegel, D. J., Finkbeiner, D. P. & Davis, M. Maps of Dust Infrared Emission for Use in Estimation of Reddening and Cosmic Microwave Background Radiation Foregrounds *Astrophys. J.* **500**, 525 (1998).

38. Schlafly, E. F. & Finkbeiner, D. P. Measuring Reddening with Sloan Digital Sky Survey Stellar Spectra and Recalibrating SFD *Astrophys. J.* **737**, 103 (2011).

39. Riello, M. *et al.* Gaia Early Data Release 3: Photometric content and validation arXiv:2012.01916 (2020).

40. Lindgren, L. *et al.* Gaia Early Data Release 3: Parallax bias versus magnitude, colour, and position arXiv:2012.01742 (2020).

41. McConnachie, A. W. The Observed Properties of Dwarf Galaxies in and around the Local Group *Astron. J.* **144**, 4 (2012).

42. Conroy, C. *et al.* Resolving the Metallicity Distribution of the Stellar Halo with the H3 Survey *Astrophys. J.* **887**, 237 (2019).

43. Harris, W. E. A Catalog of Parameters for Globular Clusters in the Milky Way *Astron. J.* **112**, 1487 (1996).

44. Astropy Collaboration *et al.* Astropy: A community Python package for astronomy *Astron. Astrophys.* **558**, A33 (2013).

45. Gravity Collaboration *et al.* A geometric distance measurement to the Galactic center black hole with 0.3% uncertainty *Astron. Astrophys.* **625**, L10 (2019).

46. Drimmel, R. & Poggio, E. On the Solar Velocity *Research Notes of the American Astronomical Society* **2**, 210 (2018).

47. Bennett, M. & Bovy, J. Vertical waves in the solar neighbourhood in Gaia DR2 *Mon. Not. R. Astron. Soc.* **482**, 1417–1425 (2019).

48. Price-Whelan, A. M. Gala: A python package for galactic dynamics *Journal of Open Source Software* **2** (2017).

49. Belokurov, V. *et al.* Precession of the Sagittarius stream *Mon. Not. R. Astron. Soc.* **437**, 116–131 (2014).

50. Górski, K. M. *et al.* HEALPix: A Framework for High-Resolution Discretization and Fast Analysis of Data Distributed on the Sphere *Astrophys. J.* **622**, 759–771 (2005).

51. Sesar, B. *et al.* Machine-learned Identification of RR Lyrae Stars from Sparse, Multi-band Data: The PS1 Sample *Astron. J.* **153**, 204 (2017).

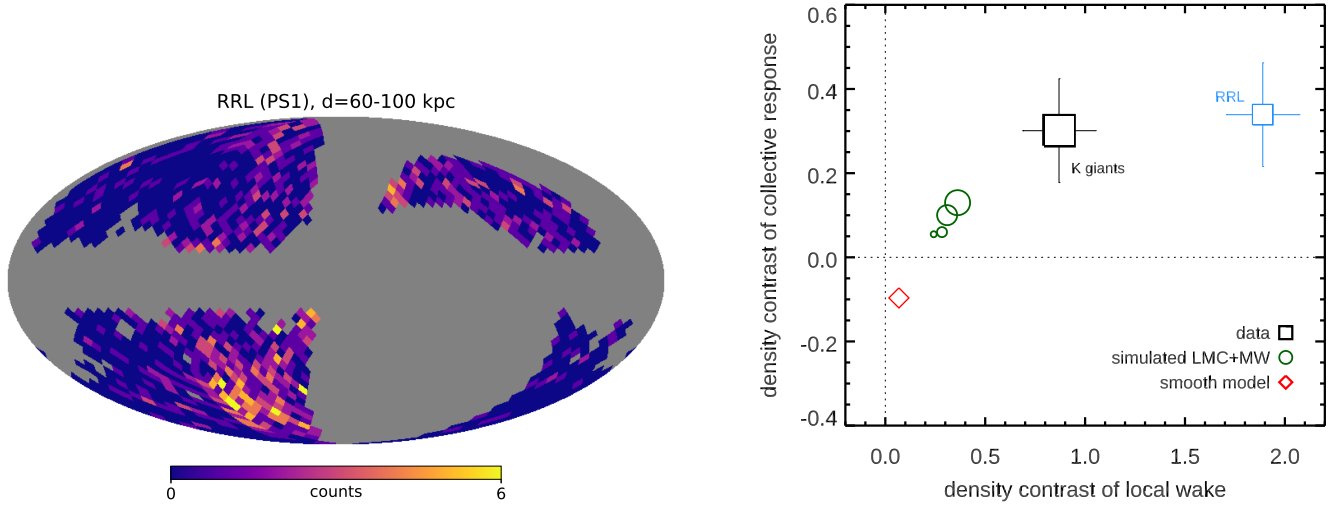
52. Rimoldini, L. *et al.* Gaia Data Release 2. All-sky classification of high-amplitude pulsating stars *Astron. Astrophys.* **625**, A97 (2019).

53. Clementini, G. *et al.* Gaia Data Release 2. Specific characterisation and validation of all-sky Cepheids and RR Lyrae stars *Astron. Astrophys.* **622**, A60 (2019).

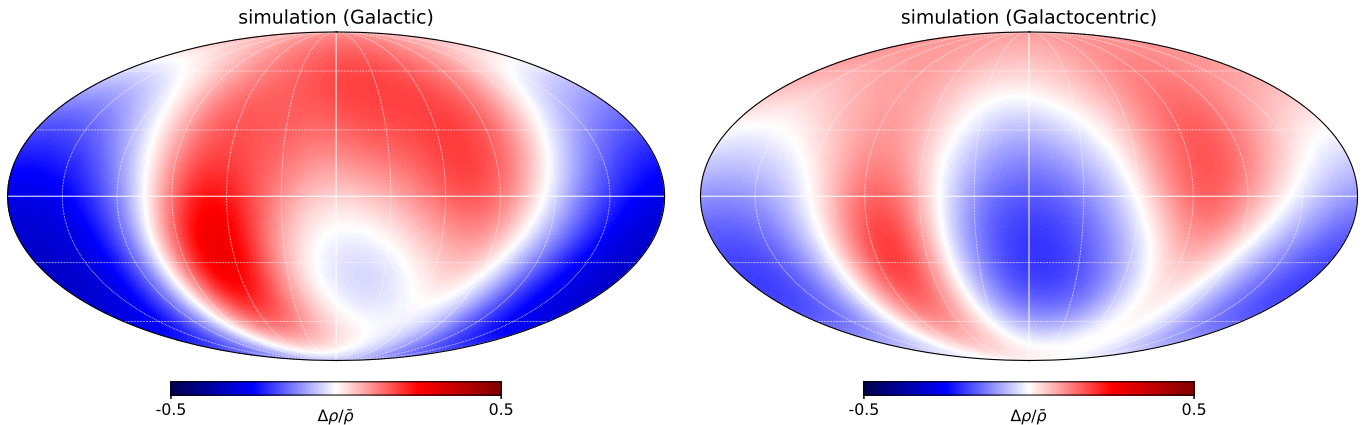
54. Mateu, C., Holl, B., De Ridder, J. & Rimoldini, L. Empirical completeness assessment of the Gaia DR2, Pan-STARRS 1, and ASAS-SN-II RR Lyrae catalogues *Mon. Not. R. Astron. Soc.* **496**, 3291–3307 (2020).

55. Hernquist, L. An Analytical Model for Spherical Galaxies and Bulges *Astrophys. J.* **356**, 359 (1990).

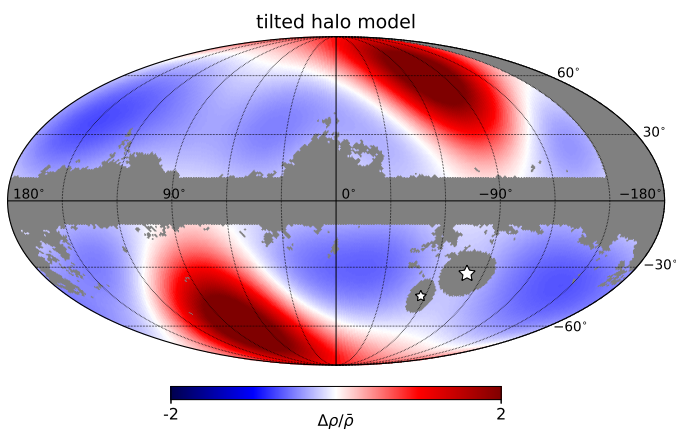
56. Yurin, D. & Springel, V. An iterative method for the construction of N-body galaxy models in collisionless equilibrium *Mon. Not. R. Astron. Soc.* **444**, 62–79 (2014).



**Extended Data Figure 7 | RR Lyrae as a probe of the stellar halo.** **Left panel:** the binned all-sky map of RR Lyrae stars identified in Pan-STARRS data<sup>51</sup>. The data are restricted to  $\text{Dec.} > -30^\circ$ . The wake is clearly visible in the lower left quadrant (compare with Extended Data Fig. 4). **Right panel:** measured densities in the wake and collective response regions for RR Lyrae (blue) compared to the K giants (black; compare with Fig. 2). Both the wake and collective response are clearly detected in the RR Lyrae.



**Extended Data Figure 8 | Predicted response of the Galactic halo to the LMC.** The  $N$ -body simulation presented in Fig. 1b is shown here without any selections, either in proper motions or on-sky (the density profile is still matched to the data, and only stars with  $60 < R_{\text{gal}} < 100$  kpc are included). **Left panel:** projection in the usual Galactic coordinates. **Right panel:** projection in Galactocentric coordinates (what an observer would see if placed at the Galactic center). In the right panel the model amplitude of the collective response is asymmetric and is largest near the Galactic plane.



**Extended Data Figure 9 | Predicted density distribution of a tilted stellar halo.** All-sky density distribution of a smooth triaxial model stellar halo that is tilted by  $60^\circ$  along the  $y$ -axis. While this model captures some of the qualitative behavior seen in the data (Fig 1a), it fails to reproduce both the detailed shape of the local wake and predicts a precise symmetry in the North and South, which is not observed.